ARTICLE OPEN

Check for updates

Computational discovery of ultra-strong, stable, and lightweight refractory multi-principal element alloys. Part I: design principles and rapid down-selection

Kate L. M. Elder [1,2✉], Joel Berry[1,2], Brandon Bocklund[1], Scott K. McCall[1], Aurélien Perron [1] and Joseph T. McKeown [1]

Refractory metal-based multi-principal element alloys (MPEAs) are compelling materials for high-temperature (1000–2000 K) structural applications. However, only a minuscule fraction of their vast and heterogeneous compositional design space has been explored, leaving many potentially interesting alloys undiscovered. In this two-part work, a large region of the 11-element Al-Cr-Fe-Hf-Mo-Nb-Ta-Ti-V-W-Zr design space is computationally explored to identify refractory MPEAs with simultaneously high yield strength or specific yield strength and body-centered cubic (BCC) solid solution stability. In *Part I*, two case studies illuminate key factors and considerations in the yield strength versus phase stability tradeoff, provide guidelines for narrowing the expansive design space, and identify many candidates predicted to be stronger than refractory MPEAs reported to date, with BCC phase stability. Our findings indicate that medium entropy ternary alloys can outperform alloys with more elements and highlight the importance of exploring regions away from the equiatomic center of composition space.

INTRODUCTION

This publication is *Part I* in the series "*Computational discovery of ultra-strong, stable, and lightweight refractory multi-principal element alloys.*"

Conventional alloys typically have one principal element with small amounts of other elements added to improve material properties[1]. A common example is steel, which contains ~98% iron with small amounts of carbon, manganese, and various other elements[2]. Multi-principal element alloys (MPEAs) consist of two or more principal elements[3] and may contain non-principal elements[4]. While conventional alloys have existed for centuries[5], MPEAs emerged in 2004 through the work of Yeh et al.[6] and Cantor et al.[7]. While prior work had assumed that alloys with more than one principal element would favor structures with brittle intermetallic phases[8], their work demonstrated that it was possible to develop solid solution MPEAs.

This realization opened the door to a vastly larger design space to explore when searching for materials with interesting properties. The inclusion of multiple principal elements can lead to materials with properties[9,10], such as high strength[11], radiation resistance[12], corrosion resistance[13], and wear resistance[14]. Since the field's inception in 2004, the volume of MPEA literature has increased exponentially[15]. However, the vast design space has not been fully explored[3], and efficient and accurate down-screening procedures are needed to discover alloys optimized for specific applications.

MPEAs based on refractory elements with high melting points, introduced in 2010[16], maintain high strength at elevated temperatures[17], making them promising candidates for applications in, e.g., aerospace[18] and hypersonics[19]. In particular, refractory MPEAs with a body-centered cubic (BCC) solid solution structure are known to have a high yield strength (YS) at elevated temperatures[20], beyond the temperature operation range for Ni-based superalloys[21].

One major challenge in the study of these alloys is the relative difficulty of synthesizing and mechanically testing them at high temperatures. A 2020 study[22] compiled mechanical property data for ~630 different MPEAs. Ninety-eight of those MPEAs consist solely of elements from the refractory-based Al-Cr-Fe-Hf-Mo-Nb-Ta-Ti-V-W-Zr family chosen for study in this work. Many of those alloys are equiatomic or close to equiatomic in composition; ~50% of the data are from tests below 100 °C, and ~75% are from tests below 1000 °C. Given the massive size of the composition plus temperature space, this modest experimental sampling has, statistically, barely scratched the surface of possibilities. A thorough search through the entire 11-element composition space can only be done with efficient computational predictions. It is highly likely that a combination of sufficiently accurate models would enable the discovery of many alloys with significantly higher strengths at elevated temperatures.

In designing stable refractory MPEAs with maximized YS at high temperatures, it is important to understand the mechanisms behind the enhanced strength of their BCC solid solution phases[4,21] and to restrict the design space to regions with sufficient phase stability. Solid solution strengthening (SSS) has been examined as a key driver of the improved refractory MPEA mechanical properties, especially at high temperatures[23–25]. Through theory, in-situ neutron-diffraction, and high-resolution transmission electron microscopy, the recent work of refs. [26,27] demonstrated that edge dislocation-based solid solution strengthening can control strength in refractory MPEAs at high temperatures. The theory developed by Maresca and Curtin in ref. [26] has been successfully applied to predict the YS of refractory BCC MPEAs whose strength is dominated by edge dislocation motion.

Machine learning has also been used as a tool to elucidate the improved mechanical properties in refractory MPEAs and for alloy

[1]Materials Science Division, Lawrence Livermore National Laboratory, Livermore, CA 94550, USA. [2]These authors contributed equally: Kate L. M. Elder, Joel Berry. ✉email: elder7@llnl.gov

down-selection. The work of ref. [28] uses feature engineering and 12 different machine learning models to investigate which descriptors are significant to describe and predict SSS. They find that electronegativity difference and shear modulus are key influencers of SSS in refractory MPEAs. A model for predicting hardness in single-phase MPEAs is also developed and applied to four different equiatomic quinary alloys. Reference [29] used convolutional neural networks (CNNs) to predict path-dependent vacancy migration energy barrier spectra, a descriptor known to be important in understanding high-temperature behavior in MPEAs[30]. They suggest that a database of this parameter could be generated with CNNs and used to screen alloys.

Designed refractory MPEAs should also generally be manufacturable in the BCC solid solution phase with sufficient phase stability over the operational regime of interest. Intermetallics, such as Laves phases, induce detrimental brittleness[31] and are thus generally necessary to avoid. The CALPHAD method can be used to predict phase stability in refractory MPEAs[32–34]. One of the guiding MPEA design principles is that the increase in entropy with the number of principal elements leads to the stabilization of solid solutions[6]. However, utilizing CALPHAD, the work of ref. [35] highlights a competing effect. The probability of selecting a pair of elements with a strong driving force for intermetallic formation (e.g., a very large atomic size difference) increases as the number of elements increases. Thus, solid solution stability is not trivially maximized by maximizing the number of elements and imposing near equiatomic compositions. Stability must be systematically assessed system by system to identify particular combinations and compositions, potentially far from equiatomic compositions, that do not produce detrimental phases.

Very recently, YS prediction combined with CALPHAD modeling has been used by Rao et al.[36] to search the 10-element Al-Cr-Hf-Mo-Nb-Ta-Ti-V-W-Zr space for promising candidates with high strength, low density, high ductility, and BCC solid solution stability. After using metallurgy insights to eliminate Al and V, every quinary equiatomic alloy in the remaining eight-element space is assessed. They found that the Hf-Mo-Nb-Ta-Ti element palette satisfied their imposed criteria and investigated the full subspace for promising candidates. Further discussion of this study in relation to the present work is provided in "Discussion".

In addition to finding refractory MPEAs with high YS, the specific yield strength (SYS) must also be considered. Alloy discovery focused on SYS is necessary for applications where mass reduction is critical. The fundamental difficulty in maximizing SYS at high temperatures stems from the correlation between higher melting temperature (needed for high-temperature operation) and higher density[21]. This adds a challenging tradeoff or dimension to the optimization problem.

Through theoretical modeling and experimental validation (presented in *Part II*), this two-part work aims to chart and understand a large part of the design space of refractory MPEAs from the Al-Cr-Fe-Hf-Mo-Nb-Ta-Ti-V-W-Zr 11-element family in terms of YS, SYS, and phase stability. Two complementary rapid design methods are proposed and applied, using the Maresca–Curtin (S)YS model[26] and CALPHAD phase stability models, as outlined in "Methods". First, all equiatomic refractory MPEAs containing two to 11 elements are studied to extract insights and design rules for alloys that maintain high YS or SYS and BCC phase stability at elevated temperatures. This approach can also serve as a quick down-screening procedure for the preliminary identification of high-performing systems. It reveals that the list of top-performing stable alloys changes considerably with temperature.

While the equiatomic down-screening procedure is rapid, it does not allow a search through the entire composition space. A Pareto optimal front approach (in (S)YS-density space), detailed in "Methods", is thus used to span the entire composition space of all ternary and quaternary systems in the 11-element palette. While applied to systems with three or four elements, the technique could easily be extended to higher-order systems. This provides a more comprehensive but still relatively rapid pathway to designing light, strong, and stable refractory MPEAs. The method also identifies top-performing alloys at low densities, which are important for weight-sensitive applications. Several high-performing ternary and quaternary alloys with predicted strengths higher than refractory MPEAs reported to date and BCC phase stability are identified for future experimental study. In this text, an N-element system from which alloys can be formed is written with dashes between elements, e.g., the ternary system Cr-Nb-W. Equiatomic alloys are written without compositional subscripts, e.g., CrNbW, and non-equiatomic alloys are written with compositional subscripts, e.g., $Cr_{20}Nb_{50}W_{30}$.

With one exception detailed below, the analysis considers only regions of design space that are 100% BCC in equilibrium, including single-phase BCC solid solutions and dual-phase (phase-separated) BCC solid solution mixtures. In alloys that are dual-phase BCC, two different phase stability conditions with respect to phase separation are considered:

- The single-phase solid solution is assumed infinitely *metastable* with respect to phase separation.
- Full phase separation to the *equilibrium* demixed compositions and phase fractions is assumed, and (S)YS is computed as an atomic phase fraction–weighted average of the (S)YS of the two equilibrium BCC phases.

The "Methods" section details each approach. The one analysis that includes regions that are not 100% BCC in equilibrium is the first "Results" subsection (titled "Yield strength trends"), a preliminary exercise to assess basic trends. Throughout the text elsewhere, only alloys that are 100% BCC are considered, and the (S)YS in alloys that are dual-phase BCC is calculated and labeled using one of the phase stability conditions described above. The label metastable or equilibrium references the treatment of dual-phase BCC alloys.

Our findings highlight the importance of predicting and systematically incorporating BCC phase stability into the design process to fully account for and optimize the tradeoff between (S)YS and phase stability, exploring regions away from the center of composition space, separately optimizing specific strength for weight-sensitive applications, and designing to specific temperature ranges, as the top-performing stable alloys can change significantly with temperature. Alloys with two BCC phases are also identified as a potentially fruitful line of further study.

RESULTS

Yield strength versus solid solution phase stability

Before performing a search over a large region of composition space, here we first outline a case study that considers a small but, in many ways, a representative subset of the composition space. The subset contains only equiatomic compositions, all 2036 equiatomic alloys with $N = 2–11$ elements that can be constructed from Al-Cr-Fe-Hf-Mo-Nb-Ta-Ti-V-W-Zr, i.e., one composition for each possible combination of elements. The purpose is to gain an understanding of the key factors and considerations in the YS/phase stability tradeoff and to extract some simple, general insights and design rules based on this understanding. The first subsection, "Yield strength trends", predicts the yield strength of all equiatomic alloys without the consideration of phase stability. This is the only section where the yield strength of alloys that are not 100% BCC is predicted.

Yield strength trends

Figure 1 shows the predicted YS and SYS of each equiatomic alloy at 1300, 1550, and 1800 K. The YS, SYS, and thermodynamics were evaluated at the stated temperature. The smaller/lighter colored
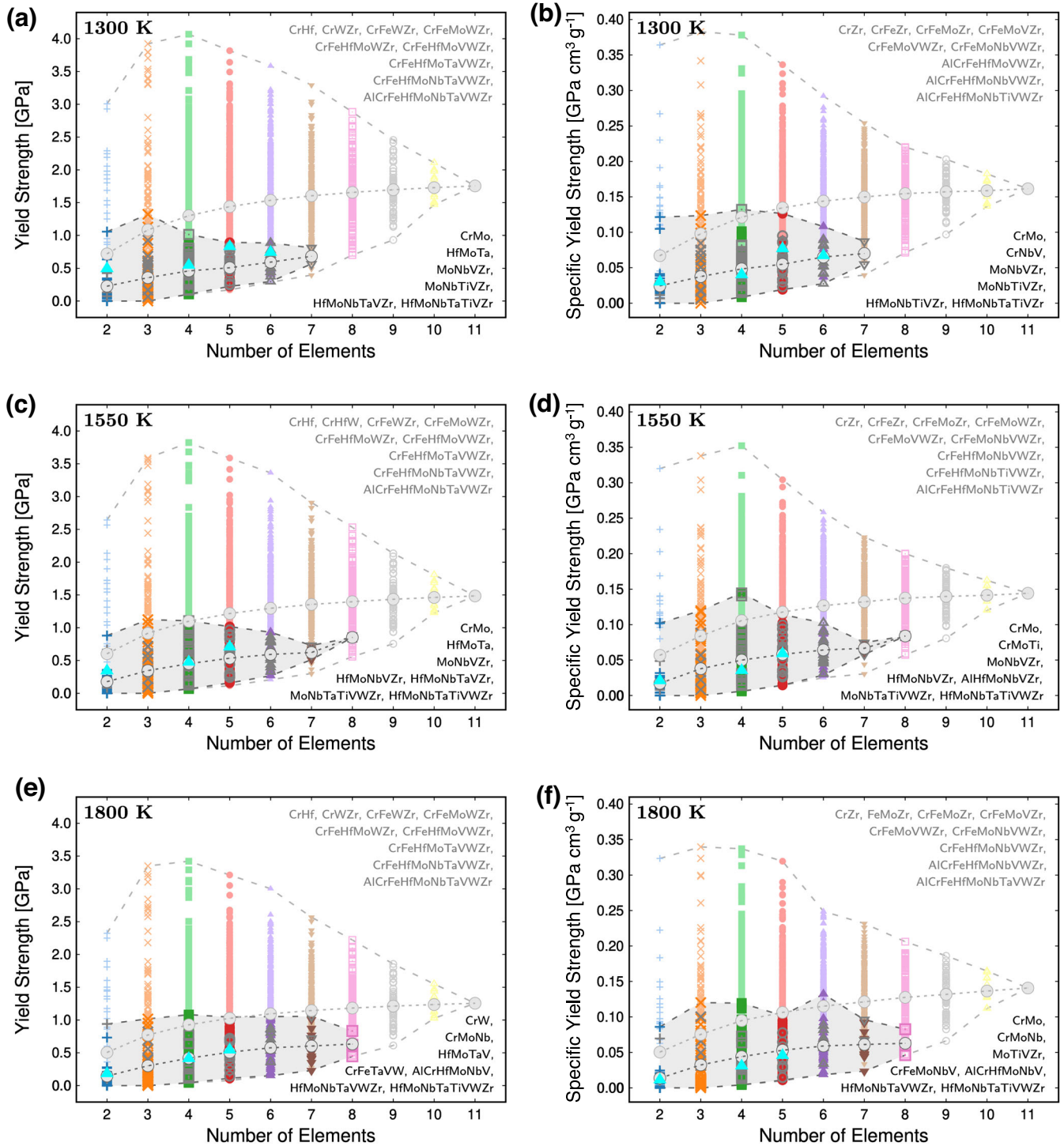
Fig. 1 Yield strength trends in equiatomic alloys. Predicted trends in **a**, **c**, **e** YS and **b**, **d**, **f** SYS versus the number of elements for all equiatomic alloys from Al-Cr-Fe-Hf-Mo-Nb-Ta-Ti-V-W-Zr at **a**, **b** 1300 K, **c**, **d** 1550 K, and **e**, **f** 1800 K. The YS, SYS, and thermodynamics were evaluated at the stated temperature. Smaller/lighter colored points show every alloy when assumed to be a BCC single-phase solid solution, no matter its equilibrium phases (single-phase BCC, dual-phase BCC, non-BCC, BCC + non-BCC). The region spanned by equilibrium single- and dual-phase BCC solid solutions is highlighted in gray. The larger/darker points (in gray shaded areas) correspond only to alloys predicted to be single-phase (colored points) or dual-phase (gray points) BCC solid solutions. Cyan triangles are reference experimental data for Ta$_{90}$W$_{10}$ (ref. [37]), MoNbTaW (ref. [20]), MoNbTaVW (ref. [20]), HfMoNbTiZr (panel (**b**) only) (ref. [38]), and MoNbTaTiVW (ref. [4]). Circular points are averages over each of the above data sets (short dashed lines are visual guides), and long dashed lines trace the envelopes of minimum and maximum strength. Listed alloys are those with the highest strength at each number of elements, N (gray text = assumed single-phase BCC, black text = BCC solid solution).

points correspond to an assumption that each alloy is a single-phase BCC solid solution, no matter its predicted phase equilibria (single-phase BCC, dual-phase BCC, non-BCC, BCC + non-BCC). This is a temporary assumption, and we acknowledge that these systems are likely to contain a non-BCC phase. The larger/darker points (gray shaded areas) correspond only to alloys predicted to be single- or dual-phase BCC solid solutions in equilibrium under the given conditions. In the gray shaded area, the yield strength of all dual-phase BCC alloys is calculated according to the equilibrium condition. Alloys for which the temperature, $T > T_{solidus}$ (75 at 1300 K, 587 at 1550 K, 1320 at 1800 K) are excluded in Fig. 1 and experimental results for notable previously studied alloys (cyan triangles) are shown for reference. $Ta_{90}W_{10}$ (ref. [37]) is taken as a representative refractory alloy that is not an MPEA, while MoNbTaW (ref. [20]), MoNbTaVW (ref. [20]), HfMoNbTiZr (ref. [38]), and MoNbTaTiVW (ref. [4]) are taken as exemplary refractory MPEAs. These alloys are all believed to be single-phase BCC solid solutions in equilibrium at the temperatures considered.

If solid solutions can always be realized and maintained (a very unrealistic but temporary assumption), the YS model predicts that four- to sixfold increases in YS and SYS over-reported values are possible. The mean solid solution strengthening (the average over all alloys of a given number of elements, N) increases monotonically with N (lighter large gray circles). Thus an equiatomic alloy made from a random selection of elements and configured as a solid solution will tend to have higher YS and SYS as the number of elements increases, but with diminishing returns as N increases.

However, the maximum solid solution strengthening among individual alloys (upper dashed line) tends to occur at $N = 3$ or 4, signaling a tradeoff between competing effects. Analysis of the YS model reveals that the key competition is between net atomic misfit volume effects, which are maximized at small N and large atomic pair misfits, and effective elastic moduli effects, which are maximized for stiff elements that tend to have intermediate atomic volumes and thus generate less misfit volume strengthening. Note that competition is not inherent in the strengthening mechanism; it results from property trends across the individual elements. For example, if the stiffer elements tended to have small or large rather than intermediate atomic volume, then misfit volume and elastic moduli effects could be maximized simultaneously, i.e., would not be mutually exclusive.

The key (dimensionless) misfit volume quantity in the theory that correlates with YS is

$$E_{mis} = \frac{1}{\overline{b}^6} \sum_{i=1}^{N} c_i (\Delta V_i)^2. \tag{1}$$

where $\overline{b}$ is the length of the alloy's Burgers vector, c_i are elemental concentrations, and ΔV_i is the misfit volume of element i. The misfit volume $\Delta V_i = V_{0i} - V$ where V_{0i} are the elemental BCC atomic volumes and the alloy volume $V = \sum_i c_i V_{0i}$. The summation term is maximized for equiatomic binary alloys that have the largest possible atomic volume difference (FeZr, FeHf, CrZr, CrHf, etc). The inclusion of $\overline{b}^6$ slightly shifts the maxima away from the equiatomic composition towards an alloy with a higher composition of the element with a smaller atomic volume. Further deviations from equiatomic compositions and added elements with intermediate atomic volumes both decrease the magnitude of E_{mis}.

The key elastic moduli quantities in the theory that correlate with YS are

$$E_{elas} = \overline{\mu}\overline{b}^3 \left(\frac{1+\overline{v}}{1-\overline{v}} \right)^{2/3} \quad \text{and} \quad \overline{\mu}\overline{b}^3 \left(\frac{1+\overline{v}}{1-\overline{v}} \right)^{4/3}. \tag{2}$$

The alloy shear modulus is calculated as $\overline{\mu} = \sqrt{\overline{C}_{44}(\overline{C}_{11} - \overline{C}_{12})/2}$ where $\overline{C}_{11}$, $\overline{C}_{12}$, and $\overline{C}_{44}$ are the alloy isotropic

elastic constants computed as $\overline{C}_{jk} = \sum_i c_i C_{jk}$. The alloy Poisson's ratio is $\overline{v} = \frac{3\overline{B} - 2\overline{\mu}}{2(3\overline{B} + \overline{\mu})}$ where the alloy bulk modulus is $\overline{B} = \frac{\overline{C}_{11} + 2\overline{C}_{12}}{3}$. E_{elas} is maximized for alloys rich in elements with the largest elemental moduli (W, Mo, Cr, etc).

The overall interpretation in terms of E_{mis} and E_{elas} is that YS is not maximized by continually increasing the number of elements; it is maximized with 3–5 elements selected and proportioned to optimize over both effects. A very simple procedure to identify strong solid solutions (ignoring for now their stability) is to

1. maximize the primary effect, misfit volume, by choosing two elements with very large misfit,
2. maximize the secondary effect, elastic modulus, by adding a very stiff third element,
3. if desired, add a fourth element with large misfit with respect to at least one element,
4. if desired, add a stiff fifth element.

Applying this procedure and quantifying stiffness in terms of $\overline{\mu}$ readily yields alloys such as CrZr, CrWZr, CrFeWZr, and CrFeMoWZr. These are the strongest or second strongest $N = 2$–5 alloys in Fig. 1a, c, e. In this case, adding W (stiff with intermediate V_0) to CrZr reduces the net misfit volume considerably, but the added stiffness strengthening is large enough to increase the overall YS from 2.93 to 3.92 GPa at 1300 K. Then adding Fe to CrWZr slightly reduces the effective modulus, but the slightly larger added misfit volume effect increases the overall YS to 4.07 GPa at 1300 K. Then adding Mo to CrFeWZr reduces the net misfit volume, but the added stiffness strengthening is insufficient to raise the overall YS, which falls to 3.82 GPa at 1300 K. Additional elements generally lower the YS at this point. The quantitative results are, of course, sensitive to the elemental properties, but the key effects and trends in YS and SYS are clear.

Solid solution phase stability trends

The above analysis ignores the thermodynamic stability of the BCC solid solution phase described by the YS model. If other non-BCC phases are present, another model is needed to predict YS. Given that other phases in these systems are likely to be ordered intermetallics that are quite strong but problematically brittle, we have chosen to restrict our analysis to alloys predicted to be 100% single- or dual-phase BCC solid solutions. This section focuses on understanding phase stability trends in refractory MPEAs. Crucially, the factors that drive solid solution strengthening due to edge dislocations directly oppose the classical Hume–Rothery rules for solid solution phase stability. Here we analyze the phase stability of the 2036 equiatomic alloys and then reconsider the YS optimization outlined above.

Figure 2a shows a scatter plot of the BCC phase fraction versus dimensionless atomic misfit volume at 1300 K. The dimensionless atomic misfit volume is given by

$$\Delta\overline{V} = \frac{4\sqrt{\sum_{i=1}^{N} c_i (\Delta V_i)^2}}{3^{3/2} \sum_{i=1}^{N} c_i V_i}. \tag{3}$$

This is related to the misfit parameter δ by $\Delta\overline{V} = \frac{4\sqrt{3}}{3}\delta$ (see ref. [39]). For simplicity, only alloys that have one BCC solid solution phase are considered. If the BCC phase fraction is less than 1, another non-BCC phase exists. A general trend of decreasing BCC phase stability with increasing misfit volume is clear for sufficiently large misfits. The maximum misfit at which 100% BCC phase is sustained is $\Delta\overline{V} \approx 0.14 - 0.15$ at 1300 K, increasing slightly to 0.164 at 1800 K (data not shown). This range may serve as a rough rule-of-thumb estimate for the largest misfit volume that can be accommodated within a stable BCC solid solution at high temperatures. One could quickly pre-screen for strong misfit-driven candidates by identifying alloys near this misfit volume
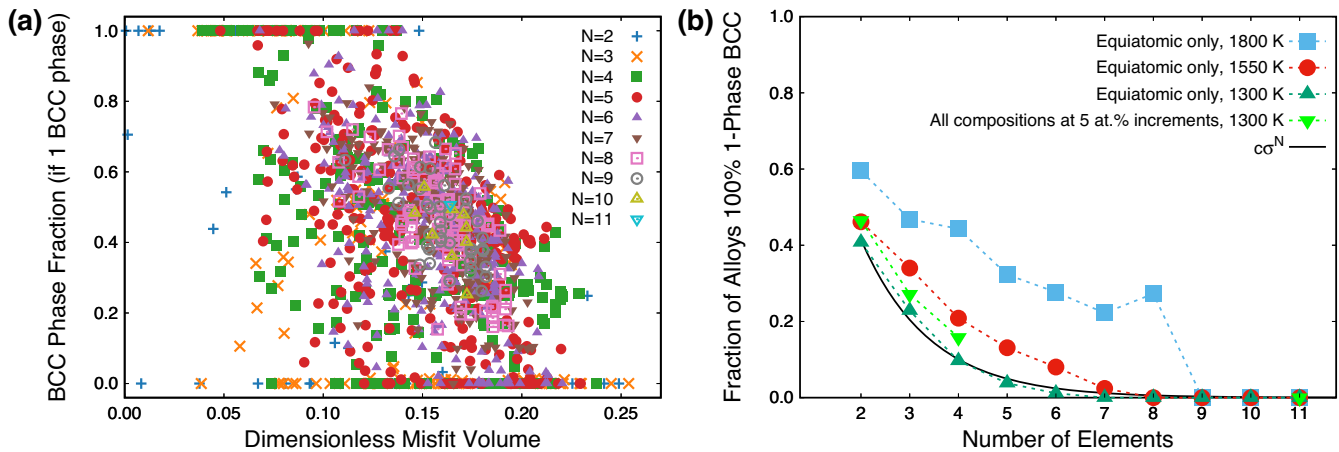
Fig. 2   Phase stability trends. Phase stability trends of all equiatomic alloys from Al-Cr-Fe-Hf-Mo-Nb-Ta-Ti-V-W-Zr. **a** Predicted BCC solid solution phase fraction of every alloy at 1300 K. Alloys above $T_{solidus}$ or with coexisting BCC solid solution phases are not shown. **b** Fraction of alloys that are 100% BCC solid solution at 1300, 1550, and 1800 K versus the number of elements N. The solid black line is a fit to $c\sigma^N$. At 1800 K, only 11 of the 165 $N = 8$ equiatomic alloys have solidus temperatures below 1800 K, thus this point has poor statistics, and none of the $N > 8$ equiatomic alloys have solidus temperatures above 1800 K, thus the sharp drop to zero.

threshold. Figure 2a also shows that equiatomic alloys with $N \geq 7$ are never 100% single-phase BCC solid solutions at 1300 K. At 1800 K, this threshold increases to $N \geq 9$ (data not shown). It has also been suggested that the misfit parameter can be used to identify when edge dislocation motion becomes the dominant strengthening mechanism (over screw dislocation motion). The authors of ref. [39] suggest this change occurs at $\Delta \bar{V} > 0.081$ ($\delta > 0.035$).

Figure 2b shows a different representation of the same effects via the fraction of all alloys predicted to be 100% single-phase BCC solid solutions versus the number of elements. Data are shown at 1300, 1550, and 1800 K for all equiatomic alloys in the 11-element family, and additional data are shown for all possible binary, ternary, quaternary, and $N = 11$ compositions (i.e., not only equiatomic) sampled at 5 at.% increments at 1300 K. This clearly shows how the probability of finding a stable solid solution decreases with increasing N, most markedly at 1300 and 1550 K. Though this finding is at odds with the concept of solid solution stabilization through configurational entropy, rationalization is fairly straightforward. As elements are added, the probability of violating the Hume–Rothery rules for solid solution phase stability increases. If N elements are chosen from the palette of 11, the odds of avoiding pairs with large enough misfit volume to destabilize the solid solution become vanishingly small as $N \to 11$. This fact was identified in ref. [35].

A simplistic statistical accounting of this effect, assuming a Gaussian probability distribution for size mismatch and a large population of elements, gives the probability of not selecting a pair with misfit above some threshold (i.e., of maintaining BCC stability) as $c\sigma^N$. Here c is a constant and $\sigma = 1 - \text{erf}(n/\sqrt{2})$ is the probability of exceeding the misfit threshold, with n the value of the threshold in units of standard deviations. Corrections can be made for a finite population of elements, but it is shown in Fig. 2b that this expression (solid black line) fits the computed 1300 K results very well. As temperature increases, the computed results shift to a notably weaker decrease versus N, indicating that another effect, presumably entropic stabilization, is emerging. However, this effect only becomes prominent at 1800 K, which is typically near or above the solidus temperature. The decrease in BCC stability with increasing N is quite rapid over most of the temperature range of interest. These phase stability trends further support the generalization that $N = 3$ is a good starting point, with additional elements then considered as specific purposes justify.

Balancing yield strength and solid solution phase stability

Given the opposing strength and stability trends outlined above, in particular those with respect to misfit volume, we now reassess the (S)YS maximization problem with the addition of phase stability constraints. The larger/darker points (in the gray shaded area) in Fig. 1 show the computed (S)YS of only alloys predicted to be 100% stable single-phase (colored points) or dual-phase (gray points) BCC solid solutions under the given conditions.

As expected, a large majority of alloys are excluded, roughly the top 85–90% in terms of predicted single-phase BCC YS and SYS. The reasons for exclusion are the presence of (1) non-BCC solid phases and (2) liquid. The percentage of alloys excluded for these reasons at 1300, 1550, and 1800 K, respectively, are (1) 87%, 58%, 20% and (2) 4%, 29%, 65%. Non-BCC solid phases are largely attributable to misfit volumes that are too large for BCC stability. Figure 1 shows that the mean solid solution strengthening among stability-screened alloys still increases monotonically with N and that the maximum strengthening among individual alloys still tends to occur at $N = 3$ or 4. However, these maxima are generally less distinct than those before stability screening, i.e., the best candidates are distributed slightly more evenly across N.

Overall, the candidates that satisfy our phase stability criteria are predicted to offer notable but less extraordinary strength gains over known alloys. Note, however, that we have only considered equiatomic compositions and that the YS model underpredicts the measured strengths of all experimentally tested alloys shown in Fig. 1. If the latter is a general trend, then actual strength gains should be larger than those indicated here.

Higher strengths can also be achieved with dual-phase BCC solid solutions that remain metastable with respect to BCC phase separation. In Fig. 1, the YS of dual-phase BCC solid solutions in the gray-shaded area is calculated according to the equilibrium condition. The YS of dual-phase BCC solid solutions can also be calculated according to the metastable condition. An analogous analysis of such dual-phase BCC metastable alloys is outlined in Supplementary Note 2 (see Supplementary Fig. 1 and Supplementary Table 1). Supplementary Table 1 reveals trends similar to those observed for dual-phase BCC equilibrium alloys but 31–42% higher maximum YS values and 2–37% higher maximum SYS values.

An alternative representation to that of Fig. 1, where the horizontal axis is density, is shown in Supplementary Fig. 1, as discussed in Supplementary Note 1. Analogous results for dual-phase BCC solid solutions that are metastable with respect to

phase separation are discussed in Supplementary Note 2 (see Supplementary Fig. 3).

Several notable insights are apparent from Fig. 1 (all insights reference alloys that are single- or dual-phase BCC solid solutions):

- YS and SYS are maximized at $N = 2$–6, consistent with received wisdom about $N > 4$–6 having negative effects on properties.
- Relatively good $N = 3$ candidates are always available, even after phase stability constraints are applied.
- The relative quality of candidates with $N \geq 4$ increases with temperature, primarily due to increases in solid solution stability.
- Dual-phase BCC solid solutions (gray points) may be very good candidates, generally below 1800 K.

Analysis of elements appearing in the strongest stable equiatomic $N = 2$–6 alloys further reveals that:

- The most common and least common elements in top alloys do not vary significantly with temperature and are nearly the same for YS and SYS.
- The most common elements (in rank order) in top alloys are typically Mo, V, Nb, and Cr. For SYS, Ti is also comparable to Nb and Cr.
- The least common elements in top alloys are distinctly Al, Fe, W, and Ta.
- The most common element pairs in top alloys are generally pairs of the most common elements.
- The least common element pairs in top alloys are generally pairs of the least common elements or pairs containing one of the least common elements.

For purposes of comparison with the detailed ternary down-selection presented in *Part II*, an analysis of elements appearing in the strongest stable equiatomic $N = 3$ alloys is provided in Supplementary Note 3. In brief, both misfit-driven and moduli-driven alloys are among the top candidates after phase stability screening. Among single-phase solid solution ternaries at 1300 K, those with the largest E_{mis} are HfMoNb, HfMoTa, and CrNbV. These are the three highest YS and SYS single-phase ternaries at 1300 K. The next four single-phase candidates (TaVW, NbVW, FeMoV, and MoTaV) have considerably smaller E_{mis} but notably larger E_{elas}. One can therefore classify the top three as misfit-driven alloys and the next four as moduli-driven or misfit- and moduli-driven alloys.

Pareto optimal front screening

The above study of equiatomic alloys demonstrated a quick but limited way to narrow down the Al-Cr-Fe-Hf-Mo-Nb-Ta-Ti-V-W-Zr search space and elucidate simple design rules. An alternate approach is to look at the Pareto optimal front in (S)YS versus density space to identify the highest-performing alloy at each density. This approach can quickly narrow down the search space and has the added benefit of identifying top performers at low densities. The equiatomic analysis identified that yield strength is maximized in systems with three or four elements. Thus, in this section, we examine the Pareto optimal fronts of all ternary (194040 alloys) and quaternary (319770 alloys) systems at all compositions (not only equiatomic) that are stable BCC solid solutions at 1300 K. The composition space of ternary and quaternary systems is evaluated in increments of 2% and 5%, respectively. Alloys of interest (AOI) along the Pareto front are identified on each plot. AOI are required to have YS > 1 GPa or SYS > 0.1 GPa cm³ g⁻¹. For each system along the Pareto front, only the alloy with the highest S(YS) is indicated. Ternary and quaternary results are then compared.

In this analysis, only alloys that consist solely of BCC solid solution phases are considered. In Figs. 3 and 4, the single-phase YS points are identical in subfigures (a) and (b), and the single-

phase SYS points are identical in subfigures (c) and (d). The labels of metastable and equilibrium refer to how the (S)YS in alloys with dual-BCC solid solution phases was calculated. The two conditions are described in the "Introduction" and "Methods" sections.

Pareto optimal ternary alloys

Figure 3 shows the (S)YS versus density calculated assuming metastable or equilibrium states for all ternary alloys from the 165 systems that are 100% BCC in equilibrium at 1300 K. The Pareto optimal front is outlined, and AOI are indicated. Blue open circles and red filled circles represent alloys that have one or two BCC phases in equilibrium, respectively. Note that single-phase (S)YS values are identical on metastable and equilibrium plots. Cyan stars represent experimental data for $Ta_{90}W_{10}$ (ref. [37]), MoNbTaVW (ref. [20]), and CrMoNbV (ref. [40]). Note that the BCC solid solution in CrMoNbV is reportedly metastable with respect to Laves phase formation for $T \lesssim 1473$ K as seen in ref. [40], while $Ta_{90}W_{10}$ and MoNbTaVW are equilibrium BCC solid solutions at the temperatures of interest.

In Fig. 3a, b, metastable alloys are those that have two BCC phases in equilibrium. These dominate the Pareto front, though a few single-phase (equilibrium) alloys appear on the front as well. Both the YS and SYS Pareto fronts contain the same five metastable systems, though not all with identical compositions, as well as the same three equilibrium AOI with identical compositions. The highest metastable alloy YS is from $Cr_{44}Nb_{20}W_{36}$ at 1.87 GPa with a density of 12.19 g cm⁻³. The highest metastable alloy SYS is from $Cr_{54}Mo_{26}Nb_{20}$ at 0.19 GPa cm³ g⁻¹ with a density of 8.24 g cm⁻³. The most prevalent elements in the eight metastable AOI are Cr, Mo, Nb, and Zr, each appearing in four systems.

For the equilibrium case (Fig. 3c, d), most alloys along the Pareto fronts have one BCC phase with, in general, lower (S)YS values than metastable Pareto front alloys. Both the YS and SYS Pareto fronts contain the same eight single-phase systems with almost identical compositions, as well as the same lone dual-phase AOI, $Cr_{42}Mo_{54}Nb_4$.

The highest equilibrium alloy YS is from $Hf_{32}Mo_{40}Ta_{28}$ at 1.53 GPa with a density of 12.97 g cm⁻³. This is lower than the maximum of 1.87 GPa for metastable alloys but is more robust as it does not rely on metastability. The Hf-Mo-Ta alloy's YS in equilibrium is ~45% higher than that of the highest reference alloy, CrMoNbV (metastable at 1300 K as seen in ref. [40]), and ~85% higher than that of the stable reference alloy MoNbTaVW (ref. [20]). The highest equilibrium alloy SYS is from $Al_{32}Fe_{58}Zr_{10}$ at 0.19 GPa cm³ g⁻¹ with a density of 5.82 g cm⁻³. This matches the best metastable alloy ($Cr_{54}Mo_{26}Nb_{20}$) but with lower density and no reliance on metastability. The Al-Fe-Zr alloy's SYS in equilibrium is ~45% higher than that of metastable CrMoNbV and ~2.75 times higher than that of MoNbTaVW (ref. [20]). The most prevalent elements in the nine equilibrium AOI are Mo (in eight systems) and Hf (in six systems). While at densities below 10 g cm⁻³, many of the metastable and equilibrium (S)YS AOI are the same, none of the (S)YS AOI at higher densities overlap, and all of the equilibrium AOI contain Hf.
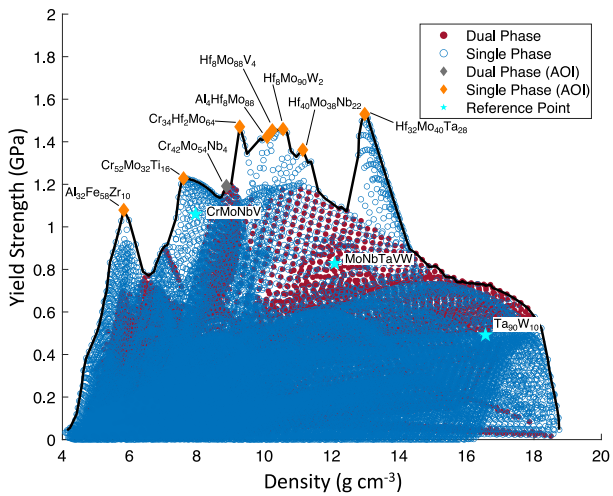
Pareto optimal quaternary alloys

The (S)YS versus density calculated assuming metastable or equilibrium states for all quaternary alloys from the 330 systems that are 100% BCC in equilibrium at 1300 K are plotted in Fig. 4. In Fig. 4a, b, metastable alloys are those that have two BCC phases in equilibrium. As with ternaries, these dominate the Pareto fronts, though a few single-phase (equilibrium) alloys appear on the front as well at very low and high densities. The highest metastable YS is from $Al_{20}Fe_{25}W_{50}Zr_5$ at 2.06 GPa with a density of 12.59 g cm⁻³. The most prevalent elements in the six metastable YS AOI are W, Zr, and Nb (in five, four, and three systems, respectively).
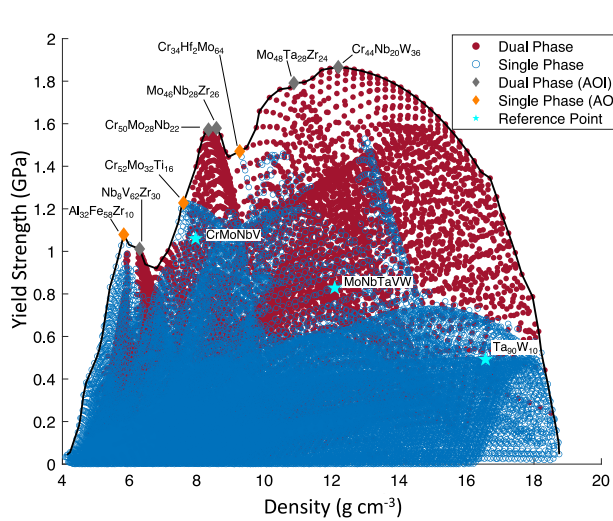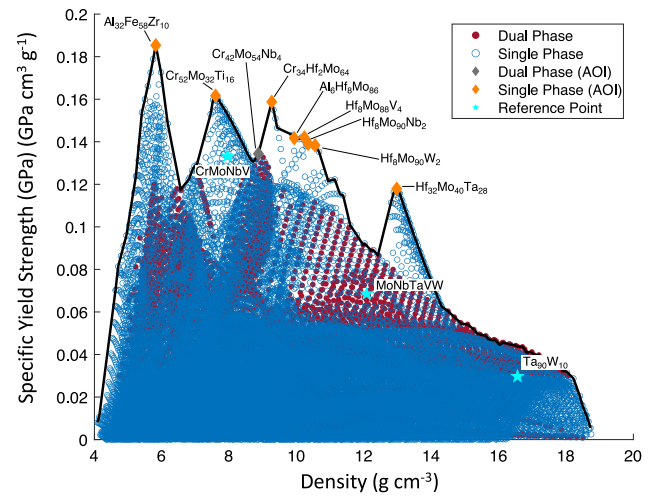
(a) Metastable - Yield Strength
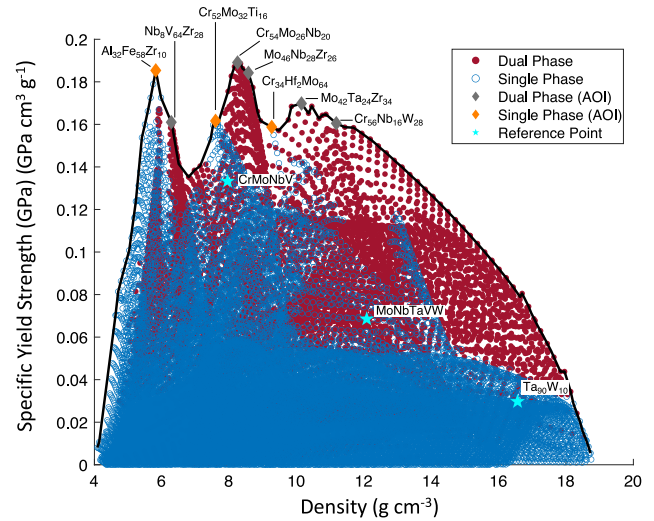
(b) Metastable - Specific Yield Strength

(c) Equilibrium - Yield Strength

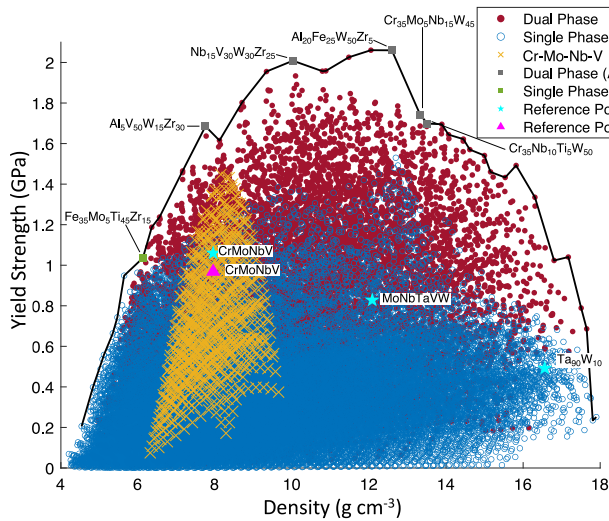**(d)** Equilibrium - Specific Yield Strength

Fig. 3 Pareto optimal analysis of ternary alloys. Plots of **a** metastable YS, **b** metastable SYS, **c** equilibrium YS, and **d** equilibrium SYS versus density for all ternary systems that are 100% BCC in equilibrium at 1300 K. Points where the alloy has one (two) BCC phase(s) in equilibrium are indicated by a blue open (red filled) circle, and the Pareto optimal front is outlined in black. Alloys of interest are identified by filled diamonds, gray for dual-phase and orange for single-phase alloys. Labeled cyan stars are reference experimental data from refs. [20,37,40].

All six AOI systems on the metastable YS plot are also on the metastable SYS plot, though Al-Fe-V-Zr (equilibrium) and Cr-Nb-V-W (metastable) also appear. The highest metastable SYS is from $Al_5V_{50}W_{15}Zr_{30}$ at 0.22 GPa cm^3 g^{-1} with a density of 7.75 g cm^{-3}. The most prevalent elements in the six metastable SYS AOI are W, Zr, Nb, and V (in six, five, four, and four systems, respectively).

For the equilibrium case (Fig. 4c, d), nearly all alloys along the Pareto fronts are single-phase BCC in equilibrium with, in general, lower (S)YS values than metastable Pareto front alloys. Two YS AOI from the Cr-Fe-Mo-Ti and Al-Cr-Hf-Mo systems are dual-BCC phase alloys. The highest equilibrium YS is from $Hf_{25}Mo_{40}Ta_{30}Zr_5$ at 1.53 GPa with a density of 12.69 g cm^{-3}. This is lower than the maximum of 2.06 GPa for metastable alloys but avoids reliance on metastability. The most prevalent elements in the 11 equilibrium YS AOI are Mo (in all 11 systems) and Hf (in six systems). This

contrasts with the prevalence of W, Zr, and Nb in top metastable alloys. The only AOI system that appears for both metastable and equilibrium conditions is Fe-Mo-Ti-Zr.

Eight AOI systems appear on both the equilibrium YS and SYS plots, while Mo-Nb-Ta-Zr, Al-Hf-Mo-Nb, and Hf-Mo-Ta-W appear only for YS and Al-Fe-V-Zr, Cr-Mo-Ti-V, Hf-Mo-Nb-Zr, and Al-Cr-Mo-Nb appear only for SYS. The highest equilibrium SYS is from $Fe_{30}Mo_{10}Ti_{45}Zr_{15}$ at 0.17 GPa cm^3 g^{-1} with a density of 6.26 g cm^{-3}. This is lower than the maximum of 0.22 GPa cm^{-3} g^{-1} for metastable alloys but with lower density and no reliance on metastability. The most prevalent elements in the 12 equilibrium SYS AOI are Mo (in 11 systems) and Hf, Cr, and Zr (each in 5 systems). This contrasts with the prevalence of W, Zr, Nb, and V in top metastable alloys.
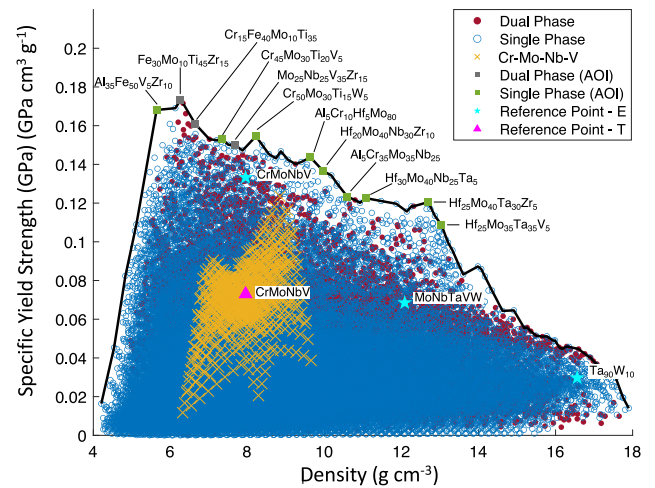
(a) Metastable - Yield Strength
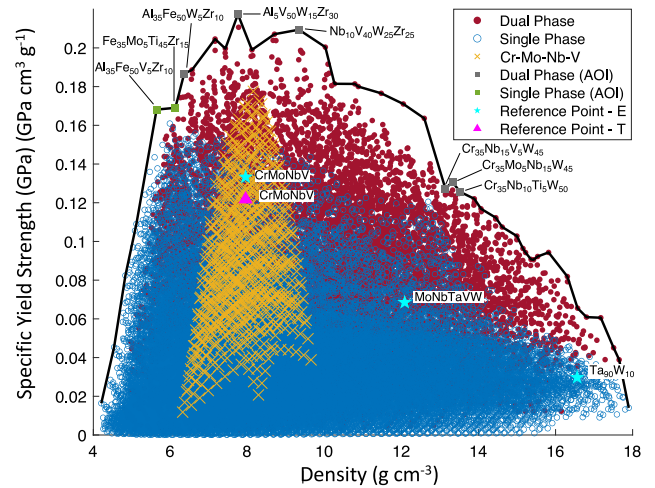
(b) Metastable - Specific Yield Strength
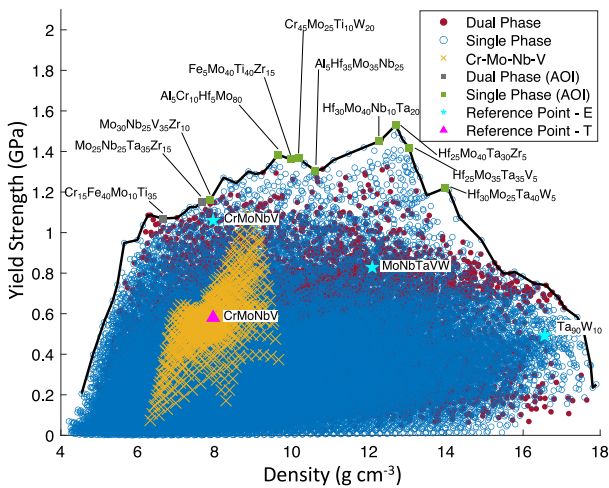
(c) Equilibrium - Yield Strength

(d) Equilibrium - Specific Yield Strength

Fig. 4 Pareto optimal analysis of quaternary alloys. Plots of **a** metastable YS, **b** metastable SYS, **c** equilibrium YS, and **d** equilibrium SYS versus density for all quaternary systems that are 100% BCC in equilibrium at 1300 K. Points where the alloy has one (two) BCC phase(s) in equilibrium are indicated by a blue open (red filled) circle, and the Pareto optimal front is outlined in black. Alloys of interest are identified by filled squares, gray for dual-phase and green for single-phase alloys. Gold × symbols highlight computed results for the Cr-Mo-Nb-V system, with labeled magenta triangles indicating equiatomic CrMoNbV (T = theory). Labeled cyan stars are experimental data from refs. [20,37,40] (E = experiment).

The Cr-Mo-Nb-V system is highlighted in Fig. 4 for three reasons. First, good agreement is observed between metastable single-phase (S)YS predictions for equiatomic CrMoNbV and experimental data[27,40], while the predicted (S)YS in dual-phase equilibrium is significantly lower. This is consistent with the single-phase microstructure observed in the experiments at 1273 K. Second, higher strengths are predicted at non-equiatomic Cr-Mo-Nb-V compositions (gold × symbols). Third, this highlights the presence of high-performing systems near but below the Pareto fronts.

A comparison of the Pareto optimal ternary and quaternary alloys is presented in Supplementary Note 4.

DISCUSSION
Equiatomic alloys
The study of two to 11-element equiatomic alloys presented highlights the key roles of atomic misfit volume and elemental elastic moduli in determining YS, as well as the subsequent conflict between maximizing YS and solid solution phase stability. Since large atomic misfits directly oppose the classical Hume–Rothery rules for solid solution phase stability, optimization over these competing effects is required. We find that this competition dramatically limits realizable strengths. Of all 2036 equiatomic alloys, the top ~85–90% in terms of predicted single-phase BCC YS and SYS were found to contain non-BCC phases at

all temperatures studied. Approximate upper limits for dimensionless misfit volume compatible with full BCC stability were found to be ~0.14–0.16, with slight temperature dependence.

The remainder of the discussion only considers alloys that consist solely of single- or dual-phase BCC solid solution phases. When discussing dual-phase BCC systems, the labels metastable and equilibrium are a reference to which condition was used to predict the (S)YS. The equiatomic analysis also reveals that, for present purposes, ternary alloys are generally as good as or better than alloys with more elements, particularly at the lower temperatures studied (~1300 K). This is consistent with the more comprehensive Pareto analysis. Near 1300 K, it thus appears that, as more elements are added, the probability of selecting a pair of elements with a strong energetic preference for intermetallic formation has a greater effect than mixing entropy, on average. As temperature increases toward 1800 K, the preference for ternary and quaternary equiatomic candidates levels off, and alloys with three to six elements become approximately equal performers. Around 1800 K, it thus appears that mixing entropy approximately balances intermetallic formation energy, on average. Above 1800 K, where mixing entropy may become dominant with strong solid solution stabilization, proximity to the melting temperature tends to preclude such a regime. This limitation is amplified by the limited number of elements with high melting temperatures; the addition of more elements is eventually likely to lower the melting temperature and make the alloy unviable.

The equiatomic analysis also shows that the top-performing stable alloys can change considerably with temperature from 1300 to 1550 to 1800 K. This indicates that a more complex optimization over a range of temperatures is needed for applications that span relatively wide temperature ranges. This is considered further in *Part II*. Mo and Hf-Mo combinations are predominant in down-selected equiatomic alloys, with HfMoTa, HfMoNb, CrMo, and MoNbVZr among the most promising candidates.

Pareto optimal alloys

The Pareto optimal front analysis provides a more comprehensive but still relatively rapid pathway to designing light, strong, and stable refractory MPEAs. In the present study, the entire composition space, instead of only equiatomic alloys, of ternary and quaternary systems at 1300 K was considered. The results demonstrate the importance of searching the entire composition space, not only the equiatomic central region. A large majority (>75%) of the AOI along the equilibrium Pareto fronts include at least one element with a relatively low atomic fraction. These high-performing alloys would be missed without considering the edges of composition space. Overall, ternary and quaternary systems were found to provide comparable candidates in terms of YS and SYS.

Several robustly stable alloys with predicted YS up to 84% higher and SYS up to 175% higher than stable alloys reported to date were identified for future experimental study, along with several metastable alloys with predicted YS up to 94% higher and SYS up to 65% higher than metastable alloys reported to date. Mo and Hf are prevalent in down-selected alloys, with alloys from the Hf-Mo-Ta(+), Hf-Mo-Nb(+), and Cr-Mo systems among the promising high YS candidates and alloys from the Al-Fe-Zr, Cr-Mo-Ti, Cr-Mo, Fe-Mo-Ti-Zr, and Al-Fe-V-Zr systems among the promising high SYS candidates. The notation (+) indicates that adding a select fourth element can yield similar performance. If metastable states can be realized (phase separation suppressed), the optimal (S)YS values are predicted to increase by between 3 and 35%.

Comparison of equiatomic and Pareto optimal alloys

The equiatomic and Pareto selection results can be compared directly for ternary and quaternary systems in equilibrium at 1300 K, as shown in Fig. 5. Since the main difference between the two techniques is the extent of composition space searched, they are likely to produce similar results only when top-performing alloys happen to be nearly equiatomic. Otherwise, the Pareto results should consist of alloys with higher strength. Figure 5 shows that YS and SYS gains available away from the equiatomic center of composition space can be very large and that the number of viable alloy systems also increases significantly.

Both selection techniques identify Hf-Mo-Ta and Hf-Mo-Nb in the top nine ternary YS and SYS systems. These are the only two YS AOI from the ternary Pareto analysis with all three elemental contents above 20%. Therefore only these two systems are likely to be present in both lists. Both selection techniques also identify Mo-Nb-V-Zr and Hf-Mo-Nb-Ta in the top 11 quaternary YS and SYS systems. These are among the most nearly equiatomic systems from the quaternary Pareto analyses.

Comparison with experimental reports

A comparison of all AOI reported here (equiatomic and Pareto) with published experimental results reveals several interesting
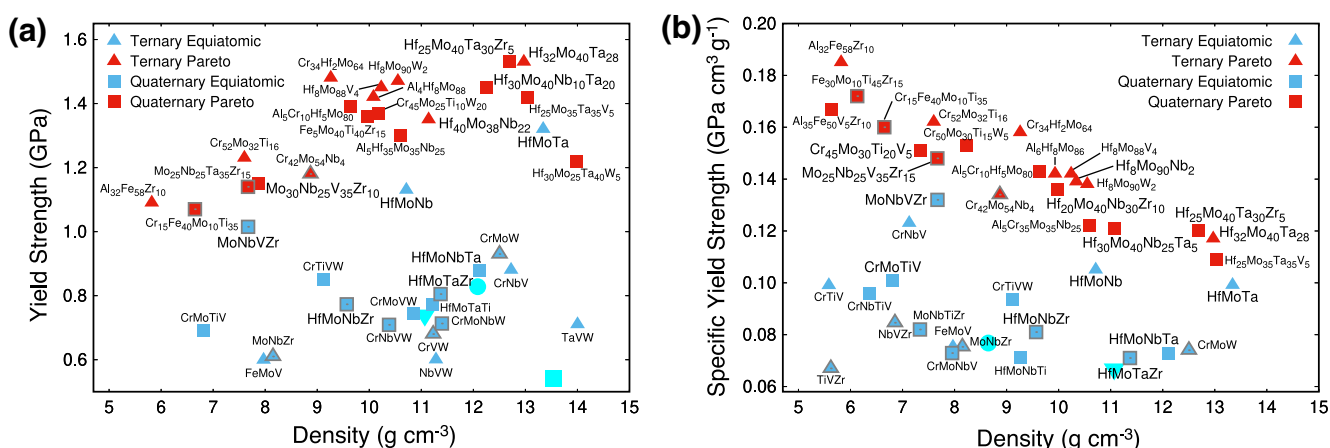

Fig. 5 Comparison of down-selected alloys. Comparison of ternary and quaternary alloys identified by equiatomic and Pareto down-selection methods. Top **a** YS and **b** SYS alloys identified by each method in equilibrium at 1300 K. Larger text labels indicate systems identified by both methods and points with gray outlines are dual-phase alloys. The cyan square, circle, and inverted triangle in (**a**) are experimental data for MoNbTaW (ref. [20]), MoNbTaVW (ref. [20]), and MoNbTaTiVW (ref. [4]), respectively. The cyan circle and inverted triangle in (**b**) are experimental data for HfMoNbTiZr (ref. [38]) and MoNbTaTiVW (ref. [4]), respectively.

facts. First, only two of our AOI, MoNbTiZr, and MoNbTiVZr, are among the 98 distinct RHEAs compiled in ref. [22]. Neither is a highly recommended AOI. MoNbTiZr is among the better equiatomic quaternaries for SYS in equilibrium at 1300 K (see Fig. 5b). MoNbTiVZr is one of the best equiatomic quinaries for YS and SYS in equilibrium at 1300 K (see Fig. 1a, b and Supplementary Fig. 1a, b and for SYS in equilibrium at 1550 K (see Supplementary Fig. 1d). However, neither alloy's predicted performance approaches that of the best Pareto optimal equilibrium alloys.

Experimental data for MoNbTiZr and MoNbTiVZr only exist at 298 K. MoNbTiZr has the highest reported room-temperature SYS ($0.218\,GPa\,cm^3\,g^{-1}$) and second-highest reported room-temperature YS (1.59 GPa) among all quaternaries in ref. [22]. MoNbTiVZr has the third-highest reported room-temperature SYS ($0.252\,GPa\,cm^3\,g^{-1}$) and seventh-highest reported room-temperature YS (1.79 GPa) among all 98 RHEAs in ref. [22]. Maresca–Curtin model predictions are in good agreement with these experimental results for both alloys, ~10% above the measured values. Thus, we expect these two alloys to perform well at 1300–1550 K but not as well as many others.

The other AOI reported here that can be found in more recent literature is CrMoNbV (refs. [27,40]). Its measured YS (1.06 GPa) and SYS ($0.133\,GPa\,cm^3\,g^{-1}$) at 1273 K are higher than those of any alloy in ref. [22]. However, given its reported metastability with respect to Laves phase formation for $T \lesssim 1473\,K$, as seen in ref. [40], we compare these results only to our metastable alloys, as shown in Supplementary Figs. 2 and 3. Our analysis does, in fact, identify CrMoNbV as a fairly promising metastable candidate for YS and SYS at 1300 K, with good agreement between predicted and measured (S)YS (as previously demonstrated in ref. [27]). However, our results indicate that several other metastable equiatomic alloys have significantly higher 1300 K (S)YS, most notably TaVWZr, NbVWZr, and MoNbVZr. And unlike CrMoNbV, these alloys (and others such as MoNbWZr) also look promising at higher temperatures, given sufficient metastability. CrMoNbV is also identified in Supplementary Fig. 1c, d as a fairly promising equilibrium candidate for YS and SYS at 1550 K, where the single-phase solid solution is predicted to be fully stable. Experimental data was not found at this temperature.

To summarize, the three AOI for which we have found experimental data show good agreement between predictions and measurements, and they are expected to perform well ~1300–1550 K (as previously confirmed for metastable CrMoNbV at 1273 K in refs. [27,40]). However, though these alloys are somewhat notable among our equiatomic AOI, none approach our Pareto optimal AOI. Thus, overall, previously studied RHEAs appear to be relatively far from optimal for operation at 1200–1800 K.

Further study

Somewhat surprisingly, both down-selection methods predict that dual-phase BCC solid solution alloys can be good candidates, especially at the lower temperatures examined and even when fully phase separated. Given the uncertainties involved in the calculation of dual-phase alloy (S)YS (see the "Yield strength model" section of "Methods"), further study is needed to accurately assess these systems.

Both the equiatomic and Pareto analyses presented here do not consider proximity to non-BCC phase boundaries in composition space. This includes liquid phases, with respect to which it is typical to limit service temperatures to below ~60% of the melting temperature. Practical usage may therefore require further compositional tuning to provide acceptable margins. These considerations are factored into the down-selection procedure presented in *Part II*. Also, though the Pareto-selected AOI identified here were restricted to the Pareto fronts, additional viable AOI can be identified near but below the fronts. Finally, some of the Pareto-selected AOI contain quite small amounts of one or more elements. Minimum elemental thresholds can be applied to remove such candidates if desired.

In the recent study by Rao et al.[36], YS prediction was similarly combined with CALPHAD modeling to identify strong, ductile, low-density, and stable single-phase BCC refractory MPEAs. Ten elements were initially considered (the 11 studied here, minus Fe). The elements Al and V are removed due to the high chance of forming an intermetallic in Al and the low oxide melting temperature of V. YS prediction and CALPHAD modeling of all equiatomic quinary alloys in the remaining eight element family is carried out to shrink the design space to the five element Hf-Mo-Nb-Ta-Ti system. Search and discovery techniques are used to identify high-performing alloys within this system. In contrast, we have directly explored a much larger region of the design space in considerable detail and have focused exclusively on strength and BCC phase stability to isolate the determinants of their (anti)correlation, develop optimization strategies, and identify preliminary sets of alloys for further study. We have also included dual-BCC phase alloys. This approach has produced a broad and diverse set of promising alloys. However, further screening or simultaneous optimization of ductility is needed to reach a point suitable for direct comparison with ref. [36]. Ductility considerations will be incorporated in future work.

Overall discussion

This work aims to establish robust procedures for the computational design of strong and stable BCC refractory MPEAs from the 11-element Al-Cr-Fe-Hf-Mo-Nb-Ta-Ti-V-W-Zr family. In *Part I*, two complementary rapid design methods are proposed and applied to explore a large part of the previously underexplored design space, with the goals of optimizing yield strength, specific yield strength, and BCC phase stability. Yield strength is computed using the Maresca–Curtin model for edge dislocation solid solution strengthening[26], and phase stability is computed using the CALPHAD method.

An analysis of all equiatomic alloys containing between two and 11 elements was used to elucidate key factors and considerations in the yield strength versus BCC phase stability tradeoff and to identify general design guidelines that can be applied to narrow the expansive design space. A more comprehensive but still relatively rapid Pareto optimal front approach was then applied to examine the entire composition space, not only equiatomic alloys, of all ternary and quaternary systems in the 11-element palette that consist solely of BCC solid solution phases. As many top-performing alloys were far from equiatomic, this method demonstrates the importance of searching all areas of composition space.

One key finding is that, in terms of combined yield strength and BCC phase stability, ternary alloys generally perform as well as or better than alloys with more elements. This is because elements beyond three generally do not significantly increase solid solution strengthening, but they can significantly decrease BCC phase stability (e.g., promote intermetallic formation), especially at relatively low temperatures (e.g., 1300 K). We also find that Mo and Hf are prevalent in down-selected alloys and that the Hf-Mo-Ta and Hf-Mo-Nb systems and related quaternaries are promising candidates, with predicted strengths higher than refractory MPEAs reported to date and BCC phase stability. Our findings highlight the importance of incorporating BCC phase stability into the design process to fully account for the strength–stability tradeoff, designing to specific temperature ranges to adequately balance significant property variations with temperature, and separately optimizing specific strength for weight-sensitive applications. Alloys with two BCC solid solution phases are also identified as a potentially fruitful area of further study.

In *Part II*, a more comprehensive design approach is developed and applied to ternary alloys, yielding several high-performing candidates that satisfy more constraints than those identified in *Part I*. Preliminary experimental validation (presented in *Part II*)

Table 1. YS model inputs. Elemental BCC elastic constants (GPa) and atomic volumes (Å^3) used as YS model inputs[26,41].

Element	C_{11}	C_{12}	C_{44}	V_0
Al	105.6	63.9	28.5	14.075
Cr	339.8	58.6	99.0	12.321
Fe	229.0	134.0	115.0	11.771
Hf	131.0	103.0	45.0	22.528
Mo	450.0	172.9	125.0	15.524
Nb	252.7	133.2	31.0	17.952
Ta	266.3	158.2	87.4	17.985
Ti	134.0	110.0	36.0	17.387
V	232.4	119.4	46.9	14.020
W	532.6	205.0	163.1	15.807
Zr	104.0	93.0	38.0	23.020

indicates that the methodology and implementation can predict key experimental trends with good quantitative accuracy. All three design approaches are compared to assess strengths and weaknesses and to verify the robustness of the design principles proposed in this work.

METHODS

Yield strength model

YS is predicted using the analytic and parameter-free mechanistic theory of Maresca and Curtin[26,27]. This model describes BCC MPEA solid solution strengthening associated with edge dislocations in terms of elemental atomic volumes and elastic moduli. The YS σ_y is calculated as

$$\sigma_y(T, \dot{\epsilon}) = \begin{cases} \sigma_{y0}\left[1 - \left(\frac{kT}{\Delta E_{b0}}\ln\frac{\dot{\epsilon}_0}{\dot{\epsilon}}\right)^{2/3}\right], \sigma_y/\sigma_{y0} \geq 0.5 \\ \sigma_{y0}\exp\left(-\frac{1}{0.55}\frac{kT}{\Delta E_{b0}}\ln\frac{\dot{\epsilon}_0}{\dot{\epsilon}}\right), \sigma_y/\sigma_{y0} < 0.5 \end{cases} \quad (4)$$

where T is temperature, $\dot{\epsilon}$ is strain rate (set to 10^{-3} s^{-1} in this work), σ_{y0} is the zero-temperature YS, k is Boltzmann's constant, ΔE_{b0} is the zero-stress energy barrier, and $\dot{\epsilon}_0$ is a reference strain rate set to 10^4 s^{-1} from ref. [26].

The zero-temperature YS is expressed as

$$\sigma_{y0} = 3.067 A_\sigma a^{-1/3}\overline{\mu}\left(\frac{1+\overline{v}}{1-\overline{v}}\right)^{4/3}\left(\sum_i \frac{c_i \Delta V_i^2}{\overline{b}^6}\right)^{2/3} \quad (5)$$

where the coefficient A_σ determined in ref. [26] is 0.04, a is a fixed-line tension coefficient set to 1/12, $\overline{\mu}$ and $\overline{v}$ are the alloy shear modulus and Poisson's ratio, c_i are elemental concentrations, ΔV_i is the misfit volume of element i, and $\overline{b}$ is the length of the alloy's Burgers vector.

The zero-stress energy barrier is given by

$$\Delta E_{b0} = A_E a^{1/3}\overline{\mu}\,\overline{b}^3\left(\frac{1+\overline{v}}{1-\overline{v}}\right)^{2/3}\left(\sum_i \frac{c_i \Delta V_i^2}{\overline{b}^6}\right)^{1/3} \quad (6)$$

where the coefficient A_E determined in ref. [26] is 2.0. The alloy shear modulus is calculated as $\overline{\mu} = \sqrt{\overline{C}_{44}(\overline{C}_{11} - \overline{C}_{12})/2}$ where $\overline{C}_{11}$, $\overline{C}_{12}$, and $\overline{C}_{44}$ are the alloy isotropic elastic constants computed as $\overline{C}_{jk} = \sum_i c_i C_{jk}$. The alloy Poisson's ratio is $\overline{v} = \frac{3\overline{B}-2\overline{\mu}}{2(3\overline{B}+\overline{\mu})}$ where the alloy bulk modulus is $\overline{B} = \frac{\overline{C}_{11}+2\overline{C}_{12}}{3}$. The misfit volume $\Delta V_i = V_{0i} - V$ where V_{0i} are the elemental BCC atomic volumes and the alloy volume $V = \sum_i c_i V_{0i}$.

The elemental BCC elastic constants and atomic volumes for all 11 elements are shown in Table 1. These are the same as used in ref. [26] except for the addition of Fe with values from ref. [41]. For a BCC crystal structure, $\overline{b} = \sqrt{3}a/2$ with lattice constant $a = 2V^{1/3}$. Alloy densities required to compute SYS were obtained via thermodynamic modeling as discussed in the "Phase stability model" section of "Methods". Experimental data validating the model predictions are presented in *Part II*.

Yield strength for different phase stability conditions

The first subsection of "Results" (titled Yield strength trends) calculates the (S)YS of every equiatomic alloy in the 11-element family assuming a single-phase BCC solid solution, no matter its predicted phase equilibria.

The remainder of the analysis considers only regions of design space that are 100% BCC in equilibrium, including single-phase BCC solid solutions and dual-phase (phase-separated) BCC solid solution mixtures. Two different phase stability conditions with respect to phase separation are considered:

- The single-phase solid solution is assumed infinitely *meta-stable* with respect to phase separation.
- Full phase separation to the *equilibrium* demixed compositions and phase fractions is assumed, and (S)YS is computed as an atomic phase fraction–weighted average of the (S)YS of the two equilibrium BCC phases.

Here, metastability is used only with respect to phase separation, as compositions with any non-BCC phases are excluded from consideration. Throughout the text, calculations are distinguished by the treatment of dual-BCC phase regions.

Metastable results can be considered approximate upper bounds on (S)YS, as they assume the strongest state is maintained. They may nonetheless underpredict (S)YS in some cases due to limitations of the model and neglect of non-solid solution strengthening effects. The same is true of results for equilibrium single-phase alloys. (S)YS results for equilibrium dual-phase alloys involve greater uncertainty. The assumption of full equilibration to the equilibrium phase-separated state, which is the weakest of the possible states, along with neglect of strengthening contributions from phase interfaces and other non-solid solution strengthening effects, may lead to underpredictions. However, the approximation of (S)YS as a phase fraction–weighted average of the two phases may, in some cases, lead to overpredictions. This is because the initial plastic yielding of the two-phase system may occur near the (S)YS of the weaker phase, depending on its volume fraction, morphology, and the distribution of elastic load between phases. Given these complexities, we employ the phase fraction–weighted average (S)YS as a median estimate, acknowledging the possibility of overprediction in some cases. This approximation is assessed further in *Part II* of this series.

Phase stability model

Multi-component composition- and temperature-dependent phase stability predictions were made using the CALPHAD (CALculation of PHAse Diagrams) method[42,43]. In the first subsection of "Results", phase stability predictions of all equimolar subsystems of the 11-component Al-Cr-Fe-Hf-Mo-Nb-Ta-Ti-V-W-Zr system were investigated at 1300, 1550, and 1800 K. In the second subsection of "Results", the composition space for all 165 ternary systems and all 330 quaternary systems of the 11 component Al-Cr-Fe-Hf-Mo-Nb-Ta-Ti-V-W-Zr system were computed on regular grids with a composition step size of 2 at.% (ternary systems) and 5 at.% (quaternary systems) at 1300 K. Calculations were performed using Thermo-Calc 2021a with the TCHEA4 database and TQ-interface[44]. At each investigated composition and temperature, the density, liquid phase fraction, BCC phase fraction, and the number of BCC phases are computed. If the number of BCC phases is more than one, the phase fraction and composition of the elements in each BCC phase are also computed.

Pareto optimal front analysis

In the second subsection of "Results", the Pareto optimal front in (S)YS versus density space is obtained for all ternary and quaternary systems in the Al-Cr-Fe-Hf-Mo-Nb-Ta-Ti-V-W-Zr family that are 100% BCC at 1300 K. The (S)YS is plotted versus density, and the Pareto optimal front is identified as the front encompassing the highest strength value at each density. Results are provided for four conditions: metastable alloy YS, metastable alloy SYS, equilibrium alloy YS, and equilibrium alloy SYS.

DATA AVAILABILITY

The data supporting the findings of this study are available within the paper and its supplementary files and are available from the corresponding author upon reasonable request.

CODE AVAILABILITY

The codes used during the current study are available from the corresponding author upon reasonable request.

REFERENCES

1. Savage, N. Striking a balance with high-entropy alloys. *Nature* **595**, S4–S5 (2021).
2. Segui, W. T. *Steel Design* (Cengage Learning, 2012).
3. Miracle, D. B. & Senkov, O. N. A critical review of high entropy alloys and related concepts. *Acta Mater.* **122**, 448–511 (2017).
4. Senkov, O. N., Gorsse, S. & Miracle, D. B. High temperature strength of refractory complex concentrated alloys. *Acta Mater.* **175**, 394–405 (2019).
5. Childe, V. G. *The Bronze Age* (Cambridge University Press, 1930).
6. Yeh, J. et al. Nanostructured high-entropy alloys with multiple principal elements: novel alloy design concepts and outcomes. *Adv. Eng. Mater.* **6**, 299–303 (2004).
7. Cantor, B., Chang, I. T. H., Knight, P. & Vincent, A. J. B. Microstructural development in equiatomic multicomponent alloys. *Mater. Sci. Eng. A* **375–377**, 213–218 (2004).
8. Greer, A. L. Confusion by design. *Nature* **366**, 303–304 (1993).
9. Tsai, M. & Yeh, J. High-entropy alloys: a critical review. *Mater. Res. Lett.* **2**, 107–123 (2014).
10. Gao, M. C., Yeh, J., Liaw, P. K. & Zhang, Y. *High Entropy Alloys: Fundamentals and Applications* (Springer, 2016).
11. Kang, B., Kong, T., Ryu, H. J. & Hong, S. H. Superior mechanical properties and strengthening mechanisms of lightweight AlxCrNbVMo refractory high-entropy alloys (x=0,0.5,1.0) fabricated by the power metallurgy process. *J. Mater. Res. Technol.* **69**, 32–41 (2021).
12. Lu, C. et al. Enhancing radiation tolerance by controlling defect mobility and migration pathways in multicomponent single-phase alloys. *Nat. Commun.* **7**, 13564 (2016).
13. Shi, Y., Yang, B. & Liaw, P. K. Corrosion-resistant high-entropy alloys: a review. *Metals* **7**, 43 (2017).
14. Cui, Y., Shen, J., Manladan, S. M., Geng, K. & Hu, S. Wear resistance of FeCoCr-NiMnAlx high-entropy alloy coatings at high temperature. *Appl. Surf. Sci.* **512**, 145736 (2020).
15. Praveen, S. & Kim, H. S. High-entropy alloys: potential candidates for high-temperature applications—an overview. *Adv. Eng. Mater.* **20**, 1700645 (2018).
16. Senkov, O. N., Wilks, G. B., Miracle, D. B., Chuang, C. P. & Liaw, P. K. Refractory high-entropy alloys. *Intermetallics* **18**, 1758–1765 (2010).
17. Li, X., Chen, C., Zheng, H., Zuo, Y. & Ong, S. P. Complex strengthening mechanisms in the NbMoTaW multi-principal element alloy. *NPJ Comput. Mater.* **6**, 70 (2020).
18. Miracle, D. B. High entropy alloys as a bold step forward in alloy development. *Nat. Commun.* **10**, 1038 (2019).
19. Senkov, O. N., Isheim, D., Seidman, D. N. & Pilchak, A. L. Development of a refractory high entropy superalloy. *Entropy* **18**, 102 (2016).
20. Senkov, O. N., Wilks, G. B., Scott, J. M. & Miracle, D. B. Mechanical properties of Nb25Mo25Ta25W25 and V20Nb20Mo20Ta20W20 refractory high entropy alloys. *Intermetallics* **19**, 698–706 (2011).
21. Senkov, O. N., Miracle, D. B., Chaput, K. J. & Couzinie, J. Development and exploration of refractory high entropy alloys—a review. *J. Mater. Res.* **33**, 3092–3128 (2018).
22. Borg, C. K. H. et al. Expanded dataset of mechanical properties and observed phases of multi-principal element alloys. *Sci. Data* **7**, 430 (2020).
23. Senkov, O. N., Scott, J. M., Senkova, S. V., Miracle, D. B. & Woodward, C. F. Microstructure and room temperature properties of a high-entropy TaNbHfZrTi alloy. *J. Alloys Compd.* **509**, 6043–6048 (2011).
24. Yao, H. W., Qiao, J. W., Hawk, H. F., Chen, M. W. & Gao, M. C. Mechanical properties of refractory high-entropy alloys: experiments and modeling. *J. Alloys Compd.* **696**, 1139–1150 (2017).
25. Chen, H. et al. Contribution of lattice distortion to solid solution strengthening in a series of refractory high entropy alloys. *Metall. Mater. Trans. A* **49**, 772–781 (2018).
26. Maresca, F. & Curtin, W. A. Mechanistic origin of high strength in refractory BCC high entropy alloys up to 1900 K. *Acta Mater.* **182**, 235–249 (2020).
27. Lee, C. et al. Strength can be controlled by edge dislocations in refractory high-entropy alloys. *Nat. Commun.* **12**, 5474 (2021).
28. Wen, C. et al. Modeling solid solution strengthening in high entropy alloys using machine learning. *Acta Mater.* **212**, 116917 (2021).
29. Fan, Z., Xing, B. & Cao, P. Predicting path-dependent diffusion barrier spectra in vast compositional space of multi-principal element alloys via convolutional neural networks. *Acta Mater.* **237**, 118159 (2022).
30. Vaidya, M., Pradeep, K., Murty, B., Wilde, G. & Divinski, S. Bulk tracer diffusion in CoCrFeNi and CoCrFeMnNi high entropy alloys. *Acta Mater.* **146**, 211–224 (2018).
31. Ding, Z. Y., He, Q. F., Chung, D. & Yang, Y. Evading brittle fracture in submicron-sized high entropy intermetallics in dual-phase eutectic microstructure. *Scr. Mater.* **187**, 280–284 (2020).
32. Shaikh, S. M., Hariharan, V. S., Yadav, S. K. & Murty, B. S. CALPHAD and rule-of-mixtures: a comparitive study for refractory high entropy alloys. *Intermetallics* **127**, 106926 (2020).
33. Gao, M. C. et al. Design of refractory high-entropy alloys. *JOM* **67**, 2653–2669 (2015).
34. Li, R., Xie, L., Wang, W. Y., Liaw, P. K. & Zhang, Y. High-throughput calculations for high-entropy alloys: a brief review. *Front. Mater. Sci.* **7**, 290 (2020).
35. Senkov, O. N., Miller, J. D., Miracle, D. B. & Woodward, C. Accelerated exploration of multi-principal element alloys with solid solution phases. *Nat. Commun.* **6**, 6529 (2015).
36. Rao, Y., Baruffi, C., De Luca, A., Leinenbach, C. & Curtin, W. A. Theory-guided design of high-strength, high-melting point, ductile, low-density, single-phase bcc high entropy alloys. *Acta Mater.* **237**, 118132 (2022).
37. Davis, J. R. *Metals Handbook Desk Edition* (CRC Press, 1998).
38. Tseng, K.-K. et al. Effects of Mo, Nb, Ta, Ti, and Zr on mechanical properties of equiatomic Hf-Mo-Nb-Ta-Ti-Zr alloys, Nb, Ta, Ti, and Zr on mechanical properties of equiatomic Hf-Mo-Nb-Ta-Ti-Zr alloys. *Entropy* **21**, 15 (2018).
39. Baruffi, C., Maresca, F. & Curtin, W. A. Screw vs. edge dislocation strengthening in body-centered-cubic high entropy alloys and implications for guided alloy design. *MRS Commun.* **12**, 1111–1118 (2023).
40. Feng, R. et al. Superior high-temperature strength in a supersaturated refractory high-entropy alloy. *Adv. Mater.* **33**, 2102401 (2021).
41. Ledbetter, H. M. & Reed, R. P. Elastic properties of metals and alloys, I. Iron, nickel, and iron-nickel alloys. *J. Phys. Chem. Ref. Data* **2**, 531 (1973).
42. Lukas, H., Fries, S. G. & Sundman, B. *Computational Thermodynamics: The Calphad Method* (Cambridge University Press, 2007).
43. Spencer, P. J. A brief history of CALPHAD. *Calphad* **32**, 1–8 (2008).
44. Andersson, J.-O., Helander, T., Höglund, L., Shi, P. & Sundman, B. Thermo-Calc & DICTRA, computational tools for materials science. *Calphad* **26**, 273–312 (2002).

AUTHOR CONTRIBUTIONS

K.L.M.E.: Conceptualization (supporting); Data curation (equal); Formal analysis (equal); Investigation (equal); Methodology (equal); Software (equal); Validation (equal); Visualization (equal); Writing/original draft preparation (equal). J.B.: Conceptualization (equal); Data curation (equal); Formal analysis (equal); Funding acquisition (supporting); Investigation (equal); Methodology (equal); Software (equal); Supervision (lead); Validation (equal); Visualization (equal); Writing/original draft preparation (equal). B.B.: Investigation (supporting). S.K.M.: Funding acquisition (supporting); Project administration (equal); Supervision (supporting). A.P.: Conceptualization (equal); Funding acquisition (supporting); Investigation (equal);

Methodology (equal); Supervision (supporting). J.T.M.: Funding acquisition (lead); Project administration (equal); Supervision (supporting).

COMPETING INTERESTS

The authors declare no competing interests.

ADDITIONAL INFORMATION